

Viscoelasticity and the dynamics of concentrated particle suspension in channel flow

Amir Esteghamatian¹ and Tamer A. Zaki^{1,†}

¹Department of Mechanical Engineering, Johns Hopkins University, Baltimore, MD 21218, USA

(Received 27 January 2020; revised 5 May 2020; accepted 22 June 2020)

The interplay of particles and viscoelasticity in turbulent channel flow is studied using direct numerical simulations. The particle concentration is moderate at 20% solid volume fraction, and the range of fluid elasticity spans from zero for Newtonian fluid to high Weissenberg numbers, $Wi = 25$. Qualitative changes in the flow dynamics are observed compared with dilute suspensions which were studied previously and are known to promote the cycles of hibernating and active turbulence. In contrast, at moderate concentration of particles, these cycles are entirely absent at the same level of fluid elasticity. In addition, instead of the commonly anticipated polymer drag reduction, a drag increase is observed when elasticity exceeds a threshold Weissenberg number. The higher drag is examined at various scales, starting from a global stress balance and down to the level of the particle microstructure. A key factor is the increase in polymer stresses, while the Reynolds shear stress is nearly eradicated. An explanation is provided by analysing the polymer conformation tensor using appropriate measures of its departure from the equilibrium state, with particular focus on the fluid in the vicinity of the particles. It is also demonstrated that viscoelasticity markedly affects both the diffusion and migration dynamics of the particles: diffusion is inhibited due to suppression of turbulent activity and, as a result, reduced mixing of particles and faster decorrelation of their motion; migration is preferential towards the channel centre, which leads to appreciable clustering in that region, which has a direct impact on the local polymer stresses.

Key words: polymers, particle/fluid flow, turbulence simulation

1. Introduction

Suspensions of solid particles are ubiquitous in environmental (landslides), industrial (waste slurries) and biological flows (blood), and their study has continued to yield new discoveries (Jeffrey & Acrivos 1976; Stickel & Powell 2005). The vast majority of previous efforts were dedicated to Newtonian suspensions, while in many applications the suspending fluid is non-Newtonian (Chhabra 2006). Viscoelasticity is a prominent non-Newtonian effect that alters the rheological and transport properties of the flow in complex and often unexpected ways, even in the absence of the particle phase. For instance, the addition of minute amounts of polymer additives to turbulent pipe flow renders the fluid viscoelastic, weakens the turbulence activity, and reduces the drag (Toms 1948). In the absence of turbulence, however, the same practice can destabilize

† Email address for correspondence: t.zaki@jhu.edu

the flow in the transitional regime (Samanta *et al.* 2013; Lee & Zaki 2017) and can give rise to elastic turbulence in the absence of inertia (Groisman & Steinberg 2000). In this study, we computationally investigate the combined effects of viscoelasticity and concentrated particle suspension on the dynamics of turbulent channel flow. We begin with a brief account of the rheological properties of viscoelastic suspensions in the absence of turbulence, followed by a summary of the effects of fluid inertia and turbulence on particle-laden flows; the latter studies being mostly limited to Newtonian fluids.

1.1. *Viscoelastic suspensions in inertialess flows*

Early theoretical developments by Einstein for dilute Newtonian suspensions in the absence of inertia predict a relative increase in the so-called effective viscosity, or the bulk shear viscosity of the mixture, at a rate of $\sim (5/2)\varphi$ where φ is the bulk solid volume fraction (Happel & Brenner 2012). Einarsson, Yang & Shaqfeh (2018) reported a correction to the Einstein relation in the same limit of dilute suspension, but when the background fluid is viscoelastic. The shear dependent rheology of such suspensions, including for Boger fluids, exhibits shear-thickening (Zarraga, Hill & Leighton 2001; Scirocco, Vermant & Mewis 2005). Two-dimensional numerical simulations confirmed this effect in disk suspensions in Oldroyd-B fluids (Hwang, Hulsen & Meijer 2004). In a linear velocity field and in the limit of Weissenberg number $Wi \equiv \dot{\gamma}\lambda \ll 1$, where $\dot{\gamma}$ and λ are the shear rate and the viscoelastic relaxation time, Koch & Subramanian (2006) theoretically explained that the contribution of particles to the bulk stress is two-fold: (i) polymer stresses modify the particle stresslet; (ii) velocity and pressure disturbances in the vicinity of the particles alter the polymer stress in the fluid. Recently, Yang & Shaqfeh (2018*a*) extended this analysis to moderate and high-Weissenberg numbers by boundary-fitted numerical simulations of a single sphere. Reportedly, the regions that contribute most to particle-induced fluid stresses are close to the sphere surface where streamlines form closed trajectories. In another effort, Yang & Shaqfeh (2018*b*) investigated suspensions at finite solid volume fractions ($\varphi < 10\%$), and concluded that particle–particle interactions have a negligible influence on the bulk rheology of the flow.

At non-dilute concentrations ($10\% < \varphi < 40\%$), previous studies reported a nonlinear relation between the effective viscosity and the solid volume fraction in both Newtonian and viscoelastic fluids (Denn & Morris 2014; Dai & Tanner 2017). For the latter, studies of filled molten polymers highlight a complex rheology which primarily depends on the diffusion time scale of fillers (Brownian or non-Brownian particles), but also their shape, concentration, and nature of the carrier fluid (see Rueda *et al.* (2017), for a review). For other non-Newtonian effects, such as variable-viscosity and yield-stress fluids, we refer the reader to the review of Tanner (2019).

1.2. *Inertial effects and turbulence*

In the presence of fluid inertia, the effective viscosity of suspensions increases. In the laminar regime, this observation is attributed to multiple effects, including the Reynolds stresses induced by particle fluctuations (Kulkarni & Morris 2008), particle and fluid phase acceleration (Rahmani, Hammouti & Wachs 2018) and anisotropy in microstructure leading to higher effective solid volume fractions (Picano *et al.* 2013). Since viscoelasticity influences both the hydrodynamic forces experienced by particles (Becker *et al.* 1994) and the local microstructure (D’Avino & Maffettone 2015), it is interesting to consider whether and how the increase in effective viscosity is influenced by viscoelastic effects in the carrier fluid.

Beyond a critical Reynolds number, transition to turbulence takes place and the shear stress increases dramatically – a phenomenon that is modulated by both finite-size particles (Matas, Morris & Guazzelli 2003) and viscoelasticity (Draad, Kuiken & Nieuwstadt 1998; Lee & Zaki 2017). Dilute particle suspensions can promote instability and sustain a turbulent state at lower Reynolds numbers than a single-phase flow (Matas *et al.* 2003; Loisel *et al.* 2013). Beyond the transitional regime, the literature on particle-turbulence interactions in a Newtonian fluid is extensive (cf. introduction by Agarwal, Brandt & Zaki (2014); Esteghamatian & Zaki (2019), for a review). In brief, the effect of particles on Newtonian turbulence primarily depends on the solid volume fraction and the relative size of particles with respect to the Kolmogorov scale. In a concentrated suspension of finite-size spherical particles in wall-bounded turbulence, the Reynolds shear stress is attenuated. However, due to the addition of particle stresses the overall drag is increased (Shao, Wu & Yu 2012; Picano, Breugem & Brandt 2015). Hence, the propensity of particles to increase the drag grows with the solid volume fraction. In viscoelastic single-phase flows, linear theory has been developed to explain the new phenomenology that arises in the vorticity dynamics of wall-bounded flows, e.g. re-energization of streaks, reverse-Orr amplification, and non-local amplification of vorticity away from curved surfaces (Page & Zaki 2014, 2015, 2016). A rigorous mathematical framework was also developed recently to derive perturbative expansion of the conformation tensor while maintaining the physical and geometrical consistency (Hameduddin, Gayme & Zaki 2019). A wealth of studies have been dedicated to the fully turbulent region (see review by White & Mungal (2008)), and the mathematical theory has shed light on the appropriate mean polymer conformation tensor and measures of the disturbances relative to that mean (Hameduddin *et al.* 2018; Hameduddin & Zaki 2019).

Very limited studies have been dedicated to the combined effects of finite-size particles, viscoelasticity and turbulence. For particles smaller than the Kolmogorov scale (in one-way coupling regime), De Lillo, Boffetta & Musacchio (2012) and Nowbahar *et al.* (2013) investigated the influence of viscoelasticity on the particle clustering. In a weakly viscoelastic duct flow, experimental findings by Zade, Lundell & Brandt (2019) reported a less effective drag reduction in the particle-laden condition compared with the single-phase counterpart. For suspensions at dilute limits ($\varphi = 5\%$), while the particles significantly contribute to the turbulence suppression, Esteghamatian & Zaki (2019) showed that they can also modify the cycles of low and high turbulence intensity which Xi & Graham (2010) termed ‘hibernating’ and ‘active’ turbulence. Extended periods of hibernating turbulence gives rise to the particles’ migration towards the channel centre, while the infrequent bursts of active turbulence redistributes the particles across the channel. Given the dual effect of particles in attenuating the Reynolds stresses while increasing the polymer stresses, the newly established momentum balance is expected to depend on the solid volume fraction. However, similar detailed studies of particle-laden viscoelastic flows at higher particle concentrations are absent from the literature – a matter that is addressed herein.

The present study reports on direct numerical simulations of particle-laden viscoelastic turbulent flows at 20% solid volume fraction and over a wide range of viscoelasticity. The computations resolve the flow at the scale of particles, and polymer forces are obtained by solving an evolution equation for the polymer conformation tensors. The flow configuration, governing equations and computational set-up are described in § 2. Drag modulations, polymer and turbulence modification, and particle dynamics are analysed in § 3. Concluding remarks are provided in § 4.

2. Flow configuration and numerical approach

The computational domain is a plane channel, where x , y and z correspond to the streamwise, wall-normal and spanwise directions (figure 1). The flow is maintained at a constant mass flux in the x direction. The bulk velocity, U_b , and the channel half-height, h , are chosen as characteristic scales. The associated Reynolds and Weissenberg numbers are $Re \equiv hU_b/\nu$ and $Wi \equiv \lambda U_b/h$, where ν and λ are the fluid total kinematic viscosity and viscoelastic relaxation time. When present, particles are spherical, their density matches that of the fluid ρ , and their diameter is denoted d_p . The bulk volume fraction is $\varphi \equiv N_p \mathcal{V}_p/\mathcal{V}_t$, where N_p , \mathcal{V}_p and \mathcal{V}_t are the total number of particles, the volume of a particle and the volume of the computational domain. The flow is periodic in the x and z directions, while a no-slip boundary condition is set at the bottom and top walls $y = \{0, 2\}$, as well as at the surfaces of particles.

The non-dimensional governing equations for the fluid velocity \mathbf{u}_f , the hydrodynamic pressure p , and the conformation tensor \mathbf{c} are

$$\nabla \cdot \mathbf{u}_f = 0, \quad (2.1)$$

$$\frac{\partial \mathbf{u}_f}{\partial t} + \mathbf{u}_f \cdot \nabla \mathbf{u}_f + \nabla p - \frac{\beta}{Re} \nabla^2 \mathbf{u}_f - \frac{1-\beta}{Re} \nabla \cdot \mathbf{T} - \mathbf{F} = 0, \quad (2.2)$$

$$\frac{\partial \mathbf{c}}{\partial t} + \mathbf{u}_f \cdot \nabla \mathbf{c} - \mathbf{c} \cdot \nabla \mathbf{u}_f - (\mathbf{c} \cdot \nabla \mathbf{u}_f)^T - \mathbf{T} = 0. \quad (2.3)$$

The solvent to total viscosity ratio is denoted $\beta \equiv \mu_s/\mu_s + \mu_p$, where μ_s and μ_p denote the solvent and polymer contributions, and \mathbf{F} represent a generic force field. Additionally, the viscoelastic stress tensor \mathbf{T} is expressed in terms of the conformation tensor with a FENE-P model,

$$\mathbf{T} \equiv \frac{1}{Wi} \left(\frac{\mathbf{c}}{\psi} - \frac{\mathbf{I}}{a} \right), \quad \psi = 1 - \frac{\text{tr}(\mathbf{c})}{L_{max}^2}, \quad a = 1 - \frac{3}{L_{max}^2}, \quad (2.4a-c)$$

where \mathbf{I} and L_{max} are the unit tensor and maximum extensibility of the polymer chains. The rigid-body motion of particles is governed by the Newton–Euler equations,

$$\mathcal{V}_p \frac{d\mathbf{u}_p}{dt} = \oint_{\partial \mathcal{V}_p} \boldsymbol{\sigma}_f \cdot \mathbf{n} \, dA + \mathbf{F}_c, \quad (2.5)$$

$$\mathcal{I}_p \frac{d\boldsymbol{\omega}_p}{dt} = \oint_{\partial \mathcal{V}_p} \mathbf{r} \times \boldsymbol{\sigma}_f \cdot \mathbf{n} \, dA, \quad (2.6)$$

where \mathbf{u}_p and $\boldsymbol{\omega}_p$ are the particle translational and angular velocities. The hydrodynamic stress tensor comprising both Newtonian and viscoelastic contributions is denoted $\boldsymbol{\sigma}_f$, while $\mathcal{V}_p = \pi d_p^3/6$ and $\mathcal{I}_p = \pi d_p^5/60$ are the dimensionless volume and moment of inertia of a spherical particle. The particle–particle and particle–wall repulsive collision forces, \mathbf{F}_c , are adopted from Glowinski *et al.* (2001), and are applied in the opposite direction to the outward unit vector \mathbf{n} at the surface.

For a detailed description of the herein-adopted numerical algorithm for simulating particle-laden viscoelastic turbulence, the reader is referred to Esteghamatian & Zaki (2019). For completeness, only the principal features of the algorithm are summarized here: the flow equations (2.1) and (2.2) are discretized using a control volume formulation and marched in time by a fractional step method (Rosenfeld, Kwak & Vinokur 1991).

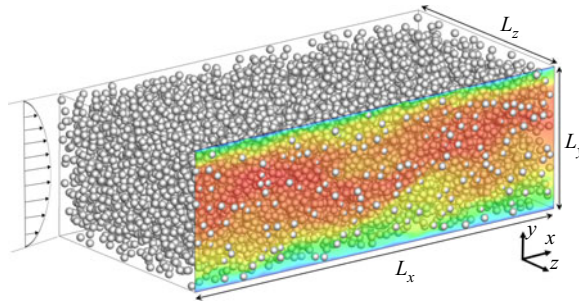


FIGURE 1. Schematic of the particle-laden flow configuration. Periodic boundary conditions are imposed in the x and z directions, and no-slip conditions $\mathbf{u}_f = 0$ are enforced at $y = \{0, 2\}$.

The diffusion terms are treated implicitly by a Crank–Nicolson scheme, while an explicit Adams–Bashforth scheme is adopted for advection. The conformation-tensor (2.3) are solved using a third-order accurate Runge–Kutta method, an explicit Adams–Bashforth discretization for advection and stretching terms and a semi-implicit approach for the polymer stress term in order to ensure finite extensibility of the polymers (Dubief *et al.* 2005; Lee & Zaki 2017). The advection term in (2.3) is evaluated with a second-order accurate spatial discretization as long as the conformation tensor remains positive definite; when its smallest eigenvalue approaches zero, the discretization is replaced by the one-sided difference which maximizes the minimum eigenvalue (see appendix B in Hameduddin *et al.* (2018)). A sharp-interface immersed boundary force field (Nicolau, Jung & Zaki 2015) is employed to enforce a no-slip boundary condition at the surface of the particles ($\mathbf{F} = \mathbf{F}_{IB}$ in (2.2)), and the conformation tensor is set to unity inside the solid domain. In addition, a short-range repulsive force equivalent to the one proposed by Glowinski *et al.* (2001) is used to avoid particle–particle and particle–wall overlap.

Our numerical method has been previously validated in single-phase Newtonian (Lee *et al.* 2013) and viscoelastic turbulence (Lee & Zaki 2017), as well as in several fluid/particle configurations in both Newtonian and viscoelastic conditions (Esteghamatian & Zaki 2019). In the Appendix, we present an additional validation case to demonstrate the accuracy of our particle-laden viscoelastic solver in the simulation of lateral migration of a sphere in Newtonian and viscoelastic fluids.

Direct numerical simulations were performed for a Newtonian and five viscoelastic fluids, each without and with the particle phase. The physical and computational parameters of the simulations are provided in table 1. In the Newtonian single-phase configuration, the friction Reynolds number $Re_\tau \equiv hu_\tau/\nu \approx 180$, where $u_\tau \equiv \sqrt{\langle \tau_w \rangle}/\rho$ denotes the friction velocity and $\langle \tau_w \rangle$ is the average wall shear stress. In particle-laden cases, the particle size in wall units $d_p\nu/u_\tau$ ranges from 18 to 21. A designation is introduced to identify each flow configuration: the letter W is followed by the Weissenberg number Wi and P by the bulk solid volume fraction of the system ϕ (%).

The computational grid was uniform in the streamwise and spanwise directions. In the wall-normal direction, the grid spacing was also uniform in the particle-laden simulations and a hyperbolic tangent grid stretching was adopted in the single-phase simulations. In order to properly capture the flow field in the vicinity of the particles, the grid-cell size in those simulation was set to $d_p/\Delta x = 16$, commensurate with earlier studies (Goyal & Derksen 2012; Costa *et al.* 2018).

Re	β, L_{max}	Wi	$\varphi(\%)$	N_p	$1/d_p$	$L_x \times L_y \times L_z$	$N_x \times N_y \times N_z$	Case	Symbol		
2800	Newtonian	0	0	0	—	$6 \times 2 \times 3$	$96 \times 192 \times 80$	W0			
			20	10 024	9	$6 \times 2 \times 3$	$864 \times 288 \times 432$	W0P20			
	FENE-P $\beta = 0.97$ $L_{max} = 70$	1	0	0	0	—	$10 \times 2 \times 4.5$	$160 \times 192 \times 120$	W1		
				20	10 024	9	$6 \times 2 \times 3$	$864 \times 288 \times 432$	W1P20		
		3	0	0	0	0	—	$10 \times 2 \times 4.5$	$160 \times 192 \times 120$	W3	
					20	10 024	9	$6 \times 2 \times 3$	$864 \times 288 \times 432$	W3P20	
		5	0	0	0	0	—	$10 \times 2 \times 4.5$	$160 \times 192 \times 120$	W5	
					20	10 024	9	$6 \times 2 \times 3$	$864 \times 288 \times 432$	W5P20	
		15	0	0	0	0	—	$10 \times 2 \times 4.5$	$160 \times 192 \times 120$	W15	
					20	10 024	9	$6 \times 2 \times 3$	$864 \times 288 \times 432$	W15P20	
		25	0	0	0	0	—	$10 \times 2 \times 4.5$	$160 \times 192 \times 120$	W25	
					20	10 024	9	$6 \times 2 \times 3$	$864 \times 288 \times 432$	W25P20	

TABLE 1. Physical and computational parameters of the simulations. Reynolds number $Re \equiv hU_b/\nu$ and Weissenberg number $Wi \equiv \lambda U_b/h$ are based on the channel half-height h , the bulk velocity U_b , total kinematic viscosity ν and viscoelastic fluid relaxation time λ . The domain sizes are $L_{\{x,y,z\}}$ in the $\{x, y, z\}$ directions, and the numbers of grid cells are $N_{\{x,y,z\}}$. The noted line types and symbols are adopted in all figures unless otherwise stated.

Randomly seeded particles naturally trigger the breakdown to turbulence in the Newtonian cases, while the single-phase Newtonian case was initialized with a superposition of laminar Poiseuille flow and random fluctuations. The viscoelastic cases were initialized with the velocity and pressure fields adopted from their Newtonian counterparts after the breakdown to turbulence.

Beyond an initial transient, once a statistically stationary state is achieved, conditional ensemble-averaging is performed in the particle and fluid phases and is denoted $\langle o_{\{f,p\}} \rangle_{\{f,p\}}$. By defining a phase indicator χ that is zero and one in the fluid and solid phases, the unconditional mixture average can be related to the phase-averaged quantities,

$$\langle o \rangle = \langle (1 - \chi)o_f \rangle + \langle \chi o_p \rangle = (1 - \phi) \langle o_f \rangle_f + \phi \langle o_p \rangle_p, \quad (2.7)$$

where ϕ denotes the solid volume fraction. For brevity, the subscripts $\{f, p\}$ are hereafter omitted from the averaging symbol. Fluctuations in fluid and particle phases are defined relative to their respective means, $o'_{\{f,p\}} = o_{\{f,p\}} - \langle o_{\{f,p\}} \rangle$. Averaging the polymer conformation tensor requires special care: owing to the Riemannian structure of the manifold of positive-definite tensors, the arithmetic mean is not physically representative of the ensemble of polymer conformation tensors. Hameduddin & Zaki (2019) proposed alternative means, namely a geometric and a log-Euclidean mean, which enable a proper representation of stretches and volume of the conformation tensor. The log-Euclidean mean, denoted $\langle \bullet \rangle_{\log}$, is adopted in this work for conditional averaging of the conformation tensors.

3. Results

Visualizations of instantaneous fields from the Newtonian (W0P20) and viscoelastic (W25P20) particle-laden simulations are provided in figure 2, and serve to highlight the striking differences between the two conditions: in the viscoelastic case, the streamwise fluid velocity is appreciably higher in the channel centre, as shown by contours of instantaneous u_f (vertical planes) and by the mean velocity profiles. Furthermore, contours

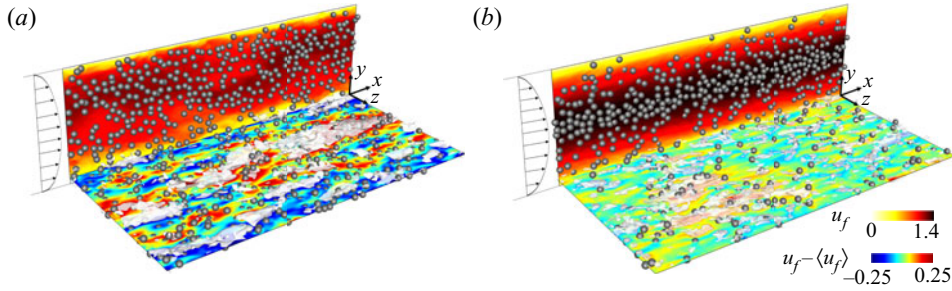


FIGURE 2. Instantaneous particles positions and contours of (side view) u_f and (top view at $y = d_p$) $u_f - \langle u_f \rangle$ for (a) Newtonian case W0P20; (b) viscoelastic case W25P20. For clarity, only particles that are cut by the planes are displayed. Isosurfaces mark (a) $u - \langle u_f \rangle = \pm 0.2$ and (b) $u - \langle u_f \rangle = \pm 0.08$ in a subregion above the horizontal plane. Wall-normal profiles of the mean streamwise fluid velocity are also schematically displayed.

of $u_f - \langle u_f \rangle$ (horizontal planes) show that the turbulence motion is highly subdued by viscoelasticity. Also, the accumulation of particles in the centre of the channel in the viscoelastic condition is a signature of their migration. In the following, we extensively analyse the state of the flow, polymers and particles in order to explain the origins of these contrasting features.

3.1. Drag modulation and stress balance

The fluid viscosity, turbulence, polymers and particle phase all contribute to the total stress within the channel. In order to assess their relative contributions, the mean total stress τ_{tot} can be expressed in terms of its constituents,

$$\begin{aligned} & \underbrace{\frac{\beta}{Re} (1 - \phi) \frac{d\langle u_f \rangle}{dy}}_{\tau_\mu} \underbrace{- [(1 - \phi) \langle u'_f v'_f \rangle + \phi \langle u'_p v'_p \rangle]}_{\tau_{Re}} \\ & + \underbrace{\frac{(1 - \beta)}{Re} (1 - \phi) \langle T_{xy} \rangle}_{\tau_\beta} + \underbrace{\phi \langle \sigma_{p,xy} \rangle}_{\tau_\phi} = \underbrace{\langle \tau_w \rangle (1 - y)}_{\tau_{tot}}. \end{aligned} \quad (3.1)$$

From left to right, the components are the viscous stress τ_μ , the turbulent Reynolds stress τ_{Re} , the polymer stress τ_β and the particle stress τ_ϕ . When integrated over $0 < y < 1$ and normalized by $0.5 \langle \tau_w \rangle^{W0}$ from the single-phase Newtonian case, the right-hand side of (3.1) reduces to $\langle \tau_w \rangle / \langle \tau_w \rangle^{W0}$, i.e. the normalized mean wall shear stress (drag), and the left-hand side expresses the contribution of different stress constituents. Figure 3 reports the normalized total drag (height of the bars) and its constituents (layering of the bars) from the various flow conditions. While the primary focus of the present work is on dense concentration ($\phi = 20\%$), for the purpose of comparison two dilute cases ($\phi = 5\%$) from Esteghamatian & Zaki (2019) are also included.

We first focus on the effect of the Weissenberg number (figure 3a). In single-phase flows, with increasing viscoelasticity, the Reynolds shear stress markedly diminishes while the polymer stress is marginally enhanced. The net effect is the well-established reduction in the total drag. At 20% particle concentration, increasing viscoelasticity results in the reduction of the Reynolds shear stress, a mild increase in the particle stress and significant enhancement of the polymer stress.

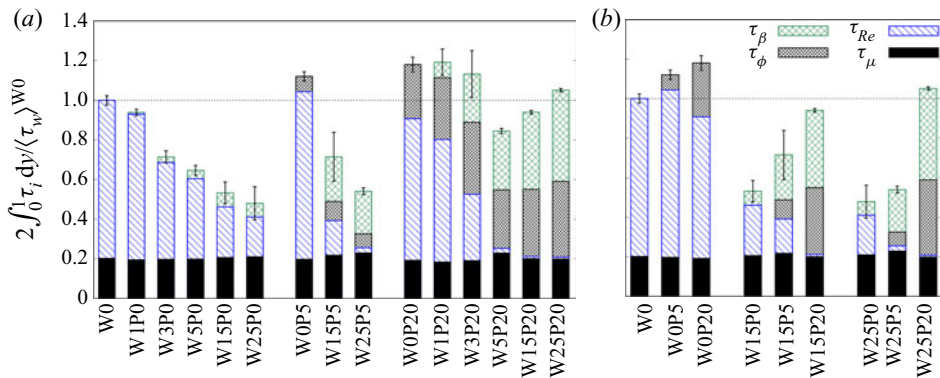


FIGURE 3. Contributions of different stress components to the total drag, integrated between $0 < y < 1$ and normalized by $0.5\langle\tau_w\rangle^{W0}$. Results are arranged to display the effect of (a) Weissenberg number, (b) solid volume fraction. The intensity of fluctuations of the total stress in time, measured by the standard deviation of $\langle\tau_w\rangle_{xz}/\langle\tau_w\rangle^{W0}$, is shown by uncertainty bars. Case designations are listed in table 1.

These combined effects give rise to a non-monotonic behaviour in the total stress: the drag is decreased with an increase in viscoelasticity up to the point where the Reynolds shear stress is nearly eradicated in case W5P20. Beyond $Wi = 5$, further increasing Wi only enhances the polymer and particle stresses and, in turn, the total drag.

The non-monotonic trend is not universal for all particle concentrations. Results from the earlier study at 5% particle concentration (Esteghamatian & Zaki 2019) predicted smaller particle and polymer stresses and lower drag relative to the 20% cases, and a consistent reduction in the total stress with increasing elasticity. The Reynolds stress, τ_{Re} , was also eradicated in the dilute case, but only at the highest Weissenberg number (case W25P5) – an indication that turbulence inhibition in particle-laden viscoelastic flows is weaker at dilute conditions. A comparison of the drag makeup at both concentrations suggests that increasing the Weissenberg number beyond $Wi = 25$ in the dilute case ($\phi = 5\%$) would enhance the polymer stress and potentially increase the total drag, although additional simulations at the lower concentration would be required to verify this outcome. Nonetheless, the general conclusion is that increasing Wi in particle-laden flows reduces drag when the reduction in τ_{Re} is appreciable, and hence τ_{Re} must be finite.

The intensity of fluctuations of the total stress in time, measured by the standard deviation of $\langle\tau_w\rangle_{xz}/\langle\tau_w\rangle^{W0}$, is shown by uncertainty bars in figure 3. Strong fluctuations in time are a signature of intermittency, or the alternation of the turbulence between a hibernating and an active state – an effect that intensifies at higher Wi . In cases where the turbulence is eradicated, the intermittency thus vanishes. At $\phi = 20\%$, the intermittency is most pronounced at $Wi = 3$. The results highlight that intermittency sets in and is most pronounced at lower Wi for larger particle concentrations.

Figure 3(b) draws the focus to the effect of the solid volume fraction on different components of the total stress. In both Newtonian and viscoelastic conditions, the addition of particles increases the total drag. In the Newtonian cases, underlying the increase in total drag is a non-monotonic behaviour of the Reynolds stress: as the particle concentration is increased, τ_{Re} first increases (W0P5) and then reduces (W0P20) relative to the single-phase configuration. This trend is consistent with a previous study in Newtonian flows and similar conditions by Picano *et al.* (2015). The increase in the total drag at higher particle concentration is more pronounced for the viscoelastic conditions due to the

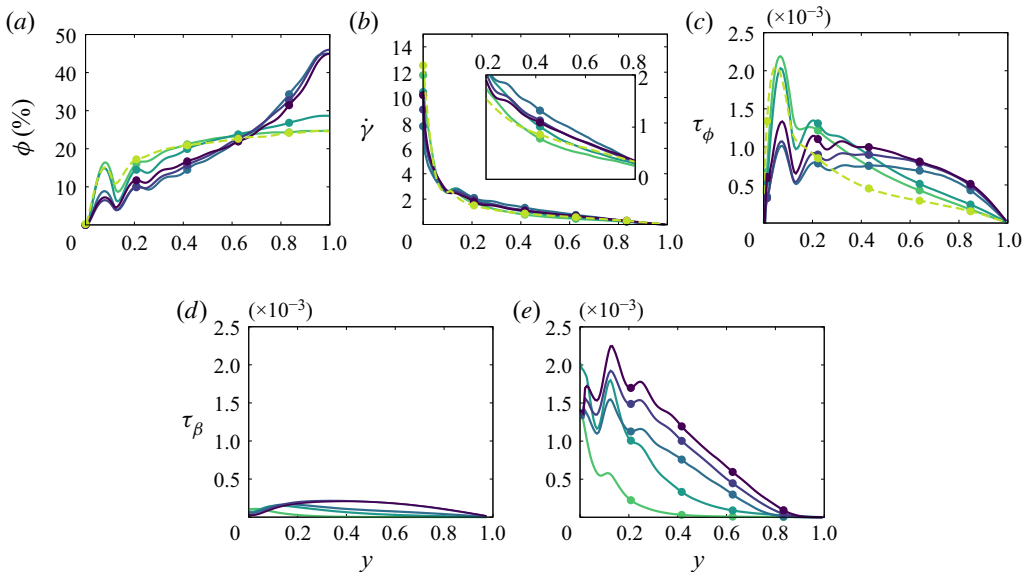


FIGURE 4. Wall-normal profiles of (a) solid volume fraction; (b) mean shear rate $\dot{\gamma} \equiv d\langle u_f \rangle / dy$ in particle-laden cases; (c) particle stress τ_ϕ ; and polymer stress τ_β in (d) single-phase and (e) particle-laden conditions. Line types are listed in table 1.

significant increase of the particle and polymer stresses with the solid volume fraction. Also, the non-monotonic trend in the Reynolds stress reported for Newtonian carrier fluids disappears in the viscoelastic cases: the addition of particles monotonically reduces and ultimately eliminates τ_{Re} .

The particle stress τ_ϕ makes an important contribution to the total drag at $\phi = 20\%$, and warrants consideration. Two relevant quantities are the solid volume fraction ϕ and the mean shear rate $\dot{\gamma} \equiv d\langle u_f \rangle / dy$ (figure 4a,b). For $Wi \geq 5$, particles migrate away from the wall in all the particle-laden cases and the solid volume fraction reaches near 45% at the channel centre (figure 4a) – an explanation of this migration trend is provided in § 3.4. In all cases, the ϕ profile has a local maximum near $y \approx d_p$, due to the asymmetric interaction of near-wall particles that are stabilized by the wall lubrication. For $Wi \geq 5$, a second local maximum near $y \approx 2d_p$ is indicative of a propensity for the particles to form a layered structure in the absence of a vertical mixing mechanism. The mean shear rate (figure 4b) exhibits a non-monotonic behaviour with increasing viscoelasticity. At the wall, it decreases to a minimum at $Wi = 5$ and increases beyond that value. Away from the wall, $y \geq 0.2$, that trend is reversed and the mean shear rate is the highest for $Wi = 5$ and decreases at higher Wi .

The profile of τ_ϕ (figure 4c) is influenced by viscoelasticity in three ways. (i) The polymers directly increase the stresslet contribution to the particle stress by altering the surface traction (Einarsson *et al.* 2018). (ii) The mean shear rates are higher in the region $y \geq 0.2$. Since particles resist deformation under shear, the stresslet contribution to the particle stress is enhanced in that region. (iii) Due to the migration of particles towards the channel centre, the particle concentration and in turn the particle stress are larger at $y \geq 0.65$. A combination of all these effects leads to the larger particle stresses in the viscoelastic cases away from the wall. Near the wall, local peaks in τ_ϕ coincide with the local maxima in the solid volume fraction. In addition, conditions with the

stronger near-wall shear rates ($Wi < 5$ cases) have larger peaks in the particle stress profiles.

The other important contribution to drag in the particle-laden viscoelastic cases is the polymer stress, especially when compared with the single-phase cases (figures 4d and 4e). The latter sustain small levels of τ_β , with very weak variation in the wall-normal direction. In contrast, in presence of the particle phase, the polymer stress increases appreciably, is highest in the near-wall region where particle layering is observed, and decays to zero towards the channel centre. Evidently, the particles contribute to the deformation of polymers and, in turn, increasing the polymer stress. It is unexpected, however, that the polymer stress vanishes in the region where the particles are most accumulated ($0.8 < y < 1.0$). In this region, the mean flow is akin to a plug profile with negligible shear rate due to the high concentration of particles (see figure 4b for the shear rate). This observation underscores that the presence of particles and of a finite shear rate are two essential components for effective polymer deformation. The differences between the polymer conformation in the near-wall region and the channel centre are further examined in § 3.3.

3.2. Flow structures and statistics

In this section, we examine the effect of particles on turbulent structures, mean flow statistics and Reynolds stresses. Figure 5 compares the instantaneous contours of $u_f - \langle u_f \rangle$, and the correlation of u_f' in the spanwise direction,

$$R_{u_f u_f'}(y, \Delta z) = \frac{\langle u_f'(x, y, z, t) u_f'(x, y, z + \Delta z, t) \rangle}{\langle u_f'(x, y, z, t) u_f'(x, y, z, t) \rangle}. \quad (3.2)$$

In single phase, relative to the Newtonian streaks, viscoelasticity inflates these structures (see figures 5a and 5b). Addition of particles to a Newtonian flow also increases the width of the streamwise structures (figure 5c). The particle-laden viscoelastic case is markedly different: the classical turbulent streaks are nearly absent at $Wi = 25$ (figure 5d), and the spanwise correlation length reduces to the order of a particle diameter.

The mean fluid-velocity profiles and their deviation from Poiseuille flow are reported in figure 6. In single-phase flows, the mean profiles monotonically approach the Poiseuille condition with increasing elasticity. In particle-laden flows, a non-monotonic behaviour that is consistent with the change in drag is observed: the flow approaches the laminar condition with increasing elasticity up to $Wi = 5$ at which the turbulence is completely eradicated. Beyond that level, the polymer stress dominates the momentum transfer in the wall-normal direction. As a result, the mean velocity profiles are flattened with further increase in elasticity.

The normal components of the Reynolds stress tensor are plotted in figure 7. In single-phase flows, the peak of $\langle u_f' u_f' \rangle$ shifts away from the wall with increasing elasticity due to the swelling of the streamwise streaks, and the stresses in the cross-flow plane are progressively attenuated at higher Wi . In particle-laden conditions, the co-presence of the solid phase and elasticity effectively suppresses the turbulent fluctuations. At $Wi \geq 5$, fluctuations are significantly suppressed in all three directions and become independent of elasticity. This observation reinforces our previous interpretation of flow perturbations (figure 5): they are not due to conventional turbulent eddies, but rather fluctuations due to the particles in shear.

Quadrant analysis of the Reynolds shear stress is reported in figure 8. The second and fourth quadrants ($\langle u_f' v_f' \rangle_{Q2}$ and $\langle u_f' v_f' \rangle_{Q4}$) are associated with ejections and sweeps that

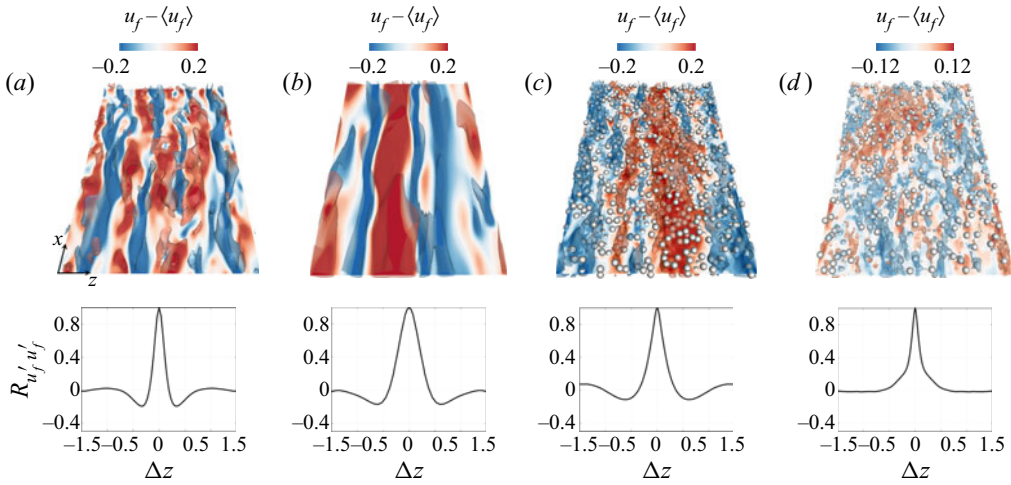


FIGURE 5. Instantaneous contours and isosurfaces of $u_f - \langle u_f \rangle$ and particle positions in xz plane (top); and two-point correlation of u'_f as a function of spanwise spacing (bottom). (a) Single-phase Newtonian (W0); (b) single-phase viscoelastic (W25); (c) particle-laden Newtonian (WOP20); (d) particle-laden viscoelastic (W25P20). The wall-normal location of the contours and correlations is $yu_\tau/\nu \approx 20$.

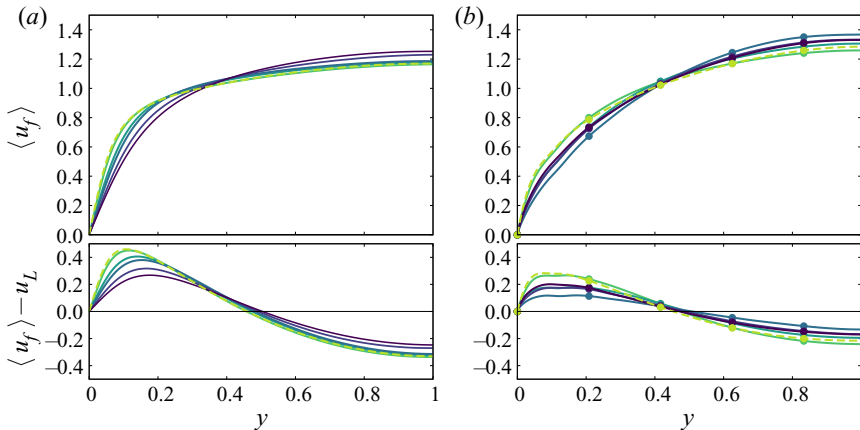


FIGURE 6. Mean streamwise fluid velocity (top); and its deviation from the laminar profile u_L (bottom) in (a) single-phase and (b) 20% particle concentration. Line types are listed in table 1.

are responsible for the turbulence production, while $\langle u'_f v'_f \rangle_{Q1}$ and $\langle u'_f v'_f \rangle_{Q3}$ correspond to interaction events that counter the wall-normal momentum flux (Wallace, Eckelmann & Brodkey 1972). In single-phase flows, elasticity reduces the magnitude of $u'_f v'_f$ in all quadrants, while the largest drops are associated with $\langle u'_f v'_f \rangle_{Q2}$ and $\langle u'_f v'_f \rangle_{Q4}$. As a result, the net effect is a reduction in the turbulent shear stress and in turn the wall-normal momentum transfer.

The addition of particles to the Newtonian flow increases the contributions in $\langle u'_f v'_f \rangle_{Q1}$, $\langle u'_f v'_f \rangle_{Q3}$ and $\langle u'_f v'_f \rangle_{Q4}$, while weakening $\langle u'_f v'_f \rangle_{Q2}$ ejection events. These modifications are marginal, and their net effect is an 11% reduction in the turbulent shear stress relative to

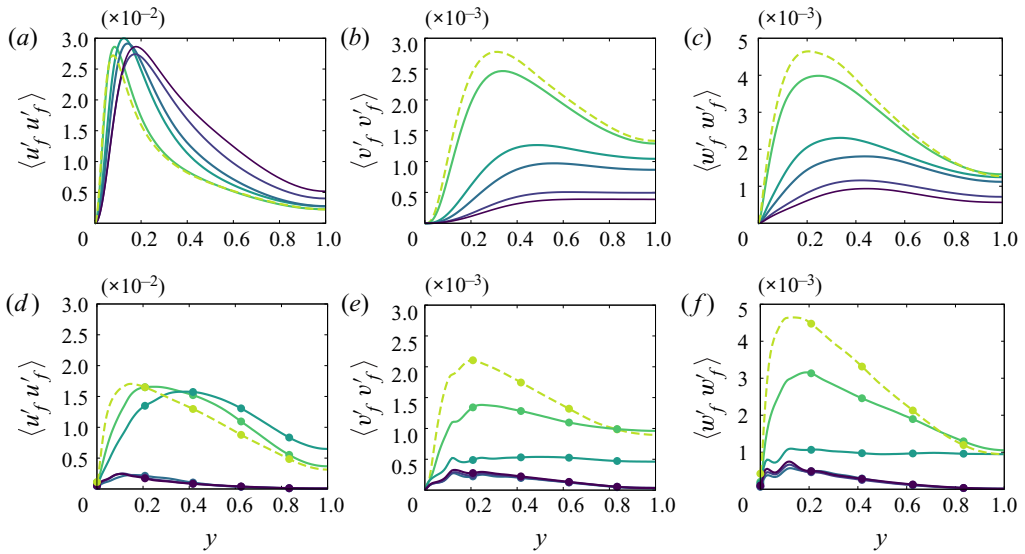


FIGURE 7. Wall-normal profiles of (a,d) streamwise, (b,e) wall-normal and (c,f) spanwise fluid velocity fluctuations. Line types are listed in table 1.

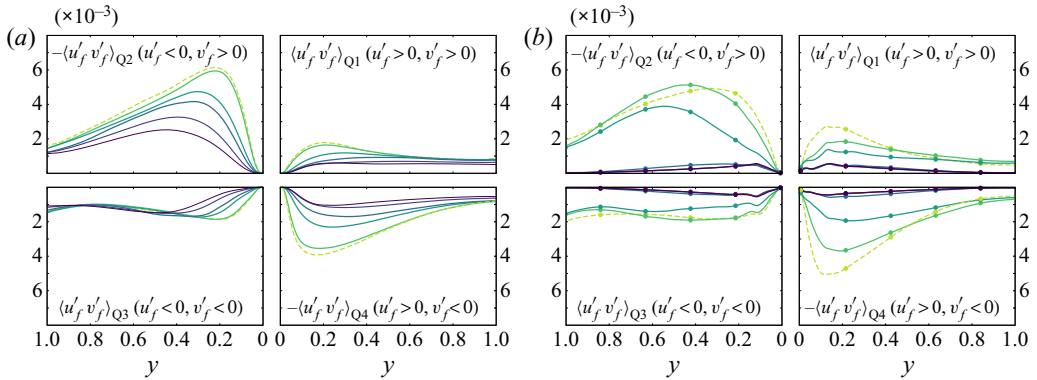


FIGURE 8. Quadrant analysis of the Reynolds shear stress, $\langle u'_f v'_f \rangle$, in (a) single-phase and (b) particle-laden conditions. Line types are listed in table 1.

the single-phase condition. At $Wi = \{1, 3\}$ the turbulence is still active, and the addition of particles results in $\{15, 31\}\%$ decrease in the turbulent shear stress mostly due to weakened $\langle u'_f v'_f \rangle_{Q2}$ ejection events. Beyond $Wi = 5$, a steep reduction in the contributions to $\langle u'_f v'_f \rangle$ is observed in all four quadrants. The nearly symmetric contributions of $\langle u'_f v'_f \rangle_{Q1}$ to $\langle u'_f v'_f \rangle_{Q4}$ highlights that the turbulence production is completely disrupted. Also, the remarkable drop in the peak values underlines the reduction in correlated motions in the x and y directions.

3.3. Polymer conformation

Velocity gradients in the fluid phase, whether induced by the mean shear, turbulent fluctuations or particles, modify the polymer conformation away from equilibrium. As

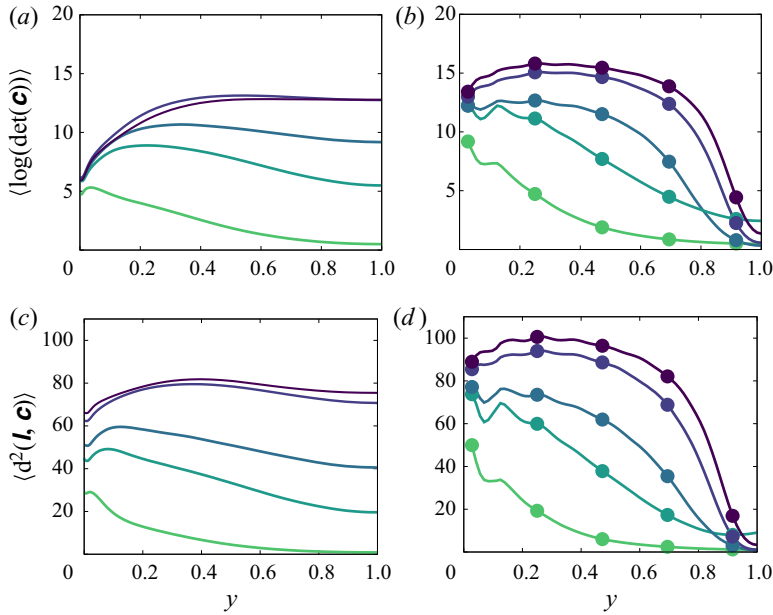


FIGURE 9. Wall-normal profiles of (a,b) average logarithmic volume and (c,d) squared geodesic distance between the conformation and the identity tensors (cf. (3.3)). Line types are listed in table 1.

explained in detail by Hameduddin *et al.* (2018), these modifications cannot be accurately interpreted with reference to isolated components of \mathbf{c} . Instead, those authors introduced three rigorous measures to characterize the conformation tensor and its perturbations: (i) the logarithmic volume ratio, $\log(\det(\mathbf{c})/\det(\bar{\mathbf{c}}))$, which compares the volume of the instantaneous polymer conformation \mathbf{c} relative to a reference conformation tensor $\bar{\mathbf{c}}$; (ii) the squared geodesic distance between \mathbf{c} and $\bar{\mathbf{c}}$ on the manifold of positive-definite matrices; (iii) the anisotropy which is a function of (i) and (ii), and therefore is not considered in the present study. The squared geodesic distance between a pair of positive-definite matrices \mathbf{A} and \mathbf{B} is defined by

$$d^2(\mathbf{A}, \mathbf{B}) \equiv \text{tr}(\log^2(\mathbf{A}^{-1/2} \cdot \mathbf{B} \cdot \mathbf{A}^{-1/2})). \quad (3.3)$$

Wall-normal profiles of the first two scalar measures are reported in figure 9, where the reference tensor was selected to be $\bar{\mathbf{c}} = \mathbf{I}$ in order to highlight the departure of the polymer from the isotropic equilibrium state. This choice of the reference state also affords a fair comparison across the different flow configurations. In both the single-phase and particle-laden cases, $\langle \log(\det(\mathbf{c})) \rangle$ and $\langle d^2(\mathbf{I}, \mathbf{c}) \rangle$ increase with Wi , with marginal difference between $Wi = 15$ and $Wi = 25$. In single-phase flows, and at the lowest Wi , the profiles of both measures decay in the outer flow due to the fast polymer relaxation away from the peak turbulence production. At the higher Wi cases, the profiles only have weak variations in the wall-normal direction. Due to the long polymers' relaxation times in these cases, the perturbations in polymer conformations are effectively transported by turbulent motion across the channel, explaining the almost uniform profile of both measures in the bulk of the channel at $Wi = \{15, 25\}$. In the particle-laden cases with $Wi \geq 5$, the wall-normal mixing is inhibited due to the suppression of turbulence (cf. figure 8b), yet both measures still exhibit small variations in most of the channel, except near the centre.

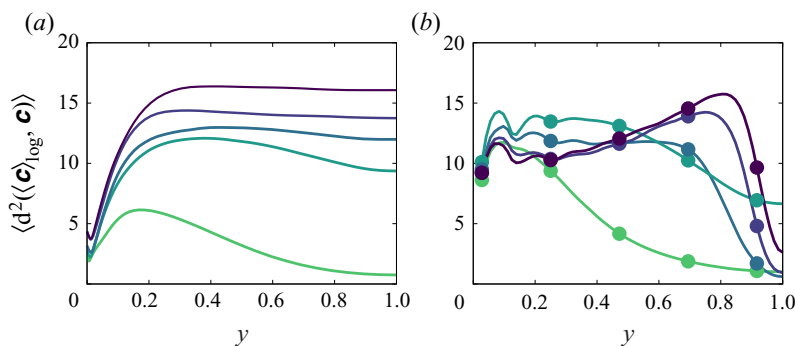


FIGURE 10. Wall-normal profiles of the mean squared geodesic distance between instantaneous and the log-Euclidean mean conformation tensors in (a) single-phase and (b) particle-laden conditions. Line types are listed [table 1](#).

The controlling factors in polymer perturbations in particle-laden cases with $Wi \geq 5$ are the mean shear rate and the particle concentration. From the wall to the centre, the polymer perturbation is enhanced with an increase in the number of particles, yet hindered by a decrease in the mean shear rate. These competing effects explain the weak variations in most of the channel. Nevertheless, near the channel centre where the mean shear decays to zero and the particles population is the highest, the significant drop in both measures of polymer deformation is a signature of a different particle–polymer interaction mechanism, which is further detailed in the following.

Profiles of $\langle d^2(\langle \mathbf{c} \rangle_{\log}, \mathbf{c}) \rangle$ are reported for the single-phase and particle-laden conditions in [figure 10](#). This quantity is the average of the squared geodesic distance between the instantaneous and the log-Euclidean mean conformation, and is therefore a measure of the intensity of the perturbation from that mean at different y locations. Note that since volumetric compressions and expansions of polymers with respect to $\langle \mathbf{c} \rangle_{\log}$ are symmetric, the average value of $\log(\det(\mathbf{c})/\det(\langle \mathbf{c} \rangle_{\log}))$ is zero and is therefore not reported. In the single-phase flows, higher elasticity is associated with larger departures of the conformation from its mean value, and the profiles of $\langle d^2(\langle \mathbf{c} \rangle_{\log}, \mathbf{c}) \rangle$ become nearly flat for $Wi \geq 5$. The recorded values are, as can be anticipated, smaller than $\langle d^2(\mathbf{I}, \mathbf{c}) \rangle$. Another notable difference is the appreciable near-wall drop in [figure 10\(a\)](#) relative to [figure 9\(c\)](#): although the polymers are highly deformed in the near-wall region, the fluctuations away from their log-Euclidean mean are relatively small. In the particle-laden cases, local maxima near the wall coincide with the peaks of the solid volume fraction profiles (cf. [figure 4a](#)). In the outer bulk flow, where the particle population is larger, the perturbations relative to the mean are enhanced at larger Wi . Nevertheless, in all cases the fluctuations decay significantly beyond $y \approx 0.8$, confirming the trends in the profiles of $\langle \log(\det(\mathbf{c})) \rangle$ and $\langle d^2(\mathbf{c}, \mathbf{I}) \rangle$ in [figures 9\(b\)](#) and [9\(d\)](#).

We now direct the focus to select y locations where we provide a further detailed account of the polymer deformation when $Wi = 25$; the results for $Wi = 15$ are qualitatively similar. [Figure 11](#) shows the joint probability density function (JPDF) of $\langle d^2(\mathbf{I}, \mathbf{c}) \rangle$ and $\log(\det(\mathbf{c}))$. At $y = 0.15$, polymers depart appreciably from the isotropic state and, in the particle-laden condition, are more deformed and expanded compared with the single-phase counterpart ([figure 11a](#)). The figure also shows instantaneous realizations of the polymer conformation, visualized using ellipsoids whose axes are the eigenvectors of the tensor each scaled by the corresponding eigenvalues; the ellipsoid are also coloured by the logarithm of the volume of the tensor. These visualizations suggest dissimilar

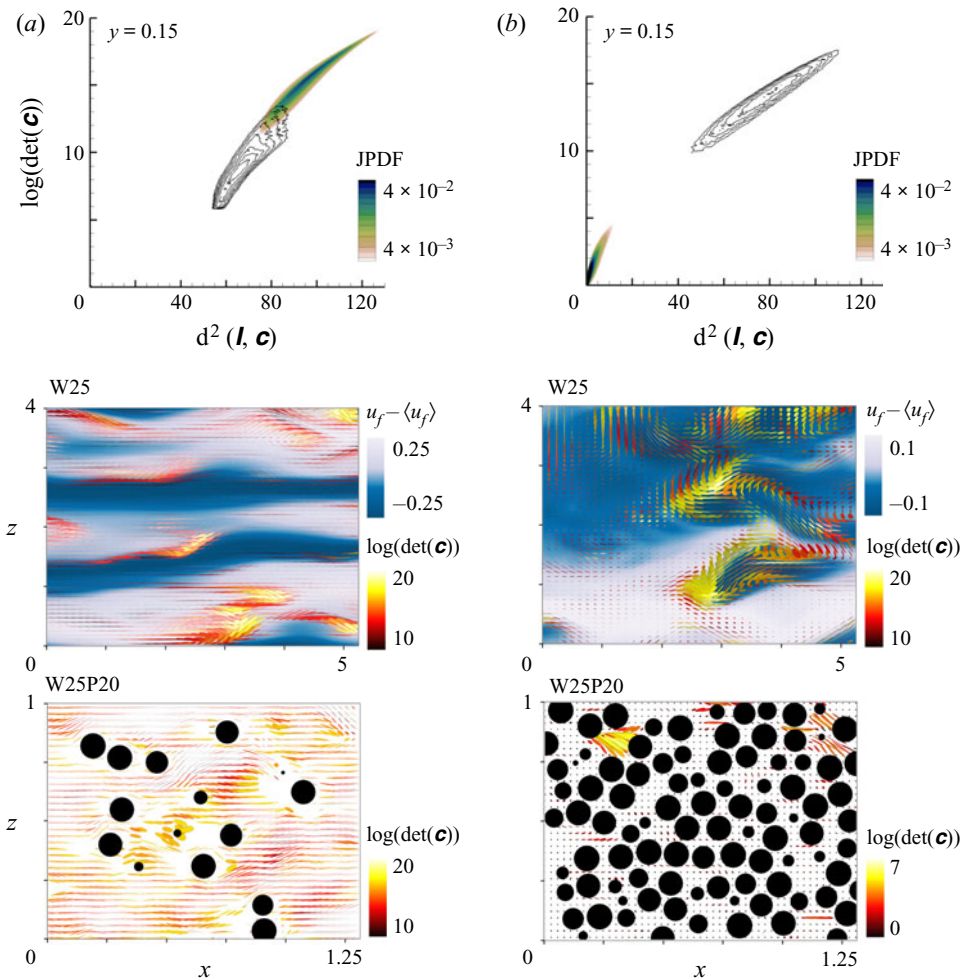


FIGURE 11. The JPDP of squared geodesic distance $d^2(\mathbf{l}, \mathbf{c})$ and the logarithmic volume $\log(\det(\mathbf{c}))$ at (a) $y = 0.15$ and (b) $y = 1$. Flood (particle-laden) and line (single-phase) contours are plotted in the same range, and refer to the cases with the $Wi = 25$ condition. Flow visualizations show snapshots of $u_f - \langle u_f \rangle$ contours in the single-phase condition and position of particles that are cut by the x - z plane in the particle-laden case. The ellipsoids represent instantaneous realizations of the polymer conformation, are coloured by the logarithmic volume of \mathbf{c} , and their axes are the eigenvectors of \mathbf{c} scaled by the corresponding eigenvalues.

mechanisms for polymers' deformation in the single-phase and particle-laden cases. In the former, polymers are most perturbed in the vicinity of the coherent turbulent structures, visualized by contours of $u_f - \langle u_f \rangle$. On the other hand, in the particle-laden condition, large polymer deformation are observed in the vicinity of particles. The JPDP of $\langle d^2(\mathbf{l}, \mathbf{c}) \rangle$ and $\log(\det(\mathbf{c}))$ at the channel centre (figure 11b) shows appreciable departure of the polymer from equilibrium in the single-phase condition. In contrast, in the particle-laden case the polymer conformation is most akin to the isotropic equilibrium state.

The instantaneous visualizations at $y = 1$ show that the polymer conformation is relatively small in volume in the two-phase case, in the confined regions between the crowd of particles. Scattered instances of deformed polymer conformation are still observable,

although their presence is rare and their magnitude is small (note that the colourbars for $\log(\det(\mathbf{c}))$ in the particle-laden condition have different ranges in figures 11a and 11b).

So far, we have shown that the particles appreciably alter the polymer deformation and, in turn, the associated stresses. We will now examine how these deformations take place at the particle scale. To this end, we first describe the particles' microstructure by evaluating the particle-pair distribution function, $q(r, \psi, \theta)$, which depends on the pair separation r , the polar angle ψ relative to the positive z axis, and the azimuthal angle θ measured anticlockwise from the positive x axis,

$$q(r, \psi, \theta) = \langle dN(r, \psi, \theta) \rangle / \langle dN(r, \psi, \theta)^R \rangle, \tag{3.4}$$

$$dN(r, \psi, \theta) = \sum_{m=1}^{N_p} \delta(r - |\mathbf{r}_m|) \delta(\psi - \psi_m) \delta(\theta - \theta_m), \tag{3.5}$$

$$\mathbf{r}_m = \mathbf{P}_m - \mathbf{P}_{ref}, \tag{3.6}$$

$$\psi_m = \cos^{-1} \left(\frac{\mathbf{r}_m \cdot \mathbf{e}_z}{|\mathbf{r}_m|} \right); \quad \theta_m = \arctan \left(\frac{\mathbf{r}_m \cdot \mathbf{e}_y}{\mathbf{r}_m \cdot \mathbf{e}_x} \right). \tag{3.7a,b}$$

The number of neighbouring particles within each bin is denoted dN , and \mathbf{P} refers to the particles' position vector. Similar to our previous study (Esteghamatian & Zaki 2019), the particle-pair distribution function q is normalized by dN^R which corresponds to a random distribution of particles with a no-overlap condition and the case-specific wall-normal profile of the mean solid fraction, in order to eliminate bias in the interpretation of the results.

Results for reference particles located at $y = 0.2$ are shown in figure 12(a). Contours of $q(r = 1.05d_p)$ are projected onto the particle surface. In terms of the particle-attached coordinates, $\tilde{\mathbf{x}} = \mathbf{x} - \mathbf{P}_{ref}$, the pairwise distribution function shows accumulations of neighbouring particles in the regions $\tilde{x}\tilde{y} < 0$ and depletion $\tilde{x}\tilde{y} > 0$. This microstructure is generally observed when finite-size particles are suspended in shear flows: particles at $\tilde{y} > 0$ advect faster than the reference one and, as a result, are more likely to accumulate behind it. A similar explanation describes the asymmetry of q with respect to the \tilde{y} axis at $\tilde{y} < 0$ locations, where the neighbouring particles advect more slowly than the reference one.

Figure 12(a) also shows the conditionally averaged log-Euclidean polymer conformation $\langle \mathbf{c} \rangle_{\log}$. In order to aid the discussion, four regions are identified within one diameter of the particle centre and are designated Ω_1 to Ω_4 . Regions Ω_1 and Ω_3 correspond to $\tilde{x}\tilde{y} > 0$, while Ω_2 and Ω_4 correspond to $\tilde{x}\tilde{y} < 0$. The conformation tensors have larger volumes in Ω_1 and Ω_3 , where polymers are effectively deformed by the presence of the reference particle and unconstrained by adjacent particles, as demonstrated by the particles microstructure. In the other two regions, where the neighbouring particles are stabilized by collision, polymers are overall less deformed and large deformations are only recorded in the immediate vicinity of the reference particle.

The effect of the microstructure on the polymer conformation in case W25P20 is quantified using the JPDP of the squared geodesic distance and logarithmic volume ratio in figure 12(b). The adopted reference conformation is $\tilde{\mathbf{c}} = \langle \mathbf{c} \rangle_{\log}$, that is to say the polymer deformation is evaluated relative to the log-Euclidean mean conformation. The line contours in both panels show the unconditional JPDP at $y = 0.15$. Near symmetry of positive and negative values of the logarithmic volume ratio confirms that the log-Euclidean mean is representative of the ensemble. The colour contours display the JPDP conditional on the fluid points belonging to specific regions: the left panel for

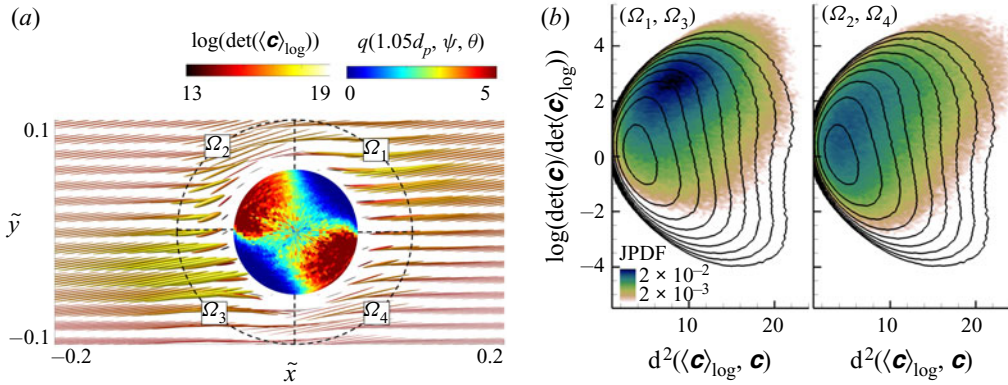


FIGURE 12. Particle-pair distribution and polymer conformation for case W25P20. (a) Reference particle located at $y = 0.2$ coloured by $q(r = 1.05d_p)$. Ellipsoids represent the particle-conditioned log-Euclidean mean conformation $\langle \mathbf{c} \rangle_{\log}$ coloured by their logarithmic volume and plotted in the particle coordinates ($\tilde{\mathbf{x}} = \mathbf{x} - \mathbf{P}_{ref}$). Four regions within one diameter from the particle centre are designated Ω_1 – Ω_4 . (b) The JPDP of squared geodesic distance $d^2(\langle \mathbf{c} \rangle_{\log}, \mathbf{c})$ and logarithmic volume ratio $\log(\det(\mathbf{c})/\det(\langle \mathbf{c} \rangle_{\log}))$ for points located at $y = 0.15$ ($\tilde{y} = -0.05$). Line contours are unconditional; colours are points within one diameter of a particle centre and exclusively located in (left) Ω_1 or Ω_3 versus (right) Ω_2 or Ω_4 .

points in Ω_1 and Ω_3 , and the right for points in Ω_2 and Ω_4 . In both figures, the colour contours are skewed towards larger values of the logarithmic volume ratio, highlighting the role of particles in the deformation of the polymers. The shift of the peak in the JPDPs towards larger expansions and squared geodesic distances is more appreciable in Ω_1 and Ω_3 , which is consistent with the interpretation of figure 12(a): polymers are more deformed in $\tilde{x}\tilde{y} > 0$ regions, where the reference particle is not immediately constrained by immediate neighbours.

3.4. Particle dynamics: diffusion and migration

The diffusion of particles is examined by evaluating their mean square displacement in the wall-normal direction $\langle \Delta y^2 \rangle$ as a function of the separation time Δt :

$$\langle \Delta y^2 \rangle \equiv \langle (P_y(t + \Delta t) - P_y(t))^2 \rangle, \tag{3.8}$$

where the average is performed over the ensemble of particles which at time t are located in a wall-parallel bin centred at y . The extent of the bin in the wall-normal direction is $1.5d_p$, while in the x and z directions it spans the full domain. The mean square displacements as a function of Δt are reported in figure 13, and exhibit quadratic and linear growth at small and large separation times, respectively. The former is indicative of correlated motion driven by collisions, and the latter is due to uncorrelated diffusive motion. In viscoelastic conditions, the eradication of turbulence results in faster decorrelation of particles motion compared with the Newtonian flow. In addition, the mean square displacements are orders of magnitude smaller in the viscoelastic flow due to the weaker mixing of particles in the wall-normal direction.

In the Newtonian condition, the first bin for the computation of $\langle \Delta y^2 \rangle$ is located at $y^+ \approx 35$. At higher wall-normal positions, and during the correlated regime $\langle \Delta y^2 \rangle \propto \Delta t^2$, the mean squared displacements weakly decrease as the turbulence activity decreases. In the

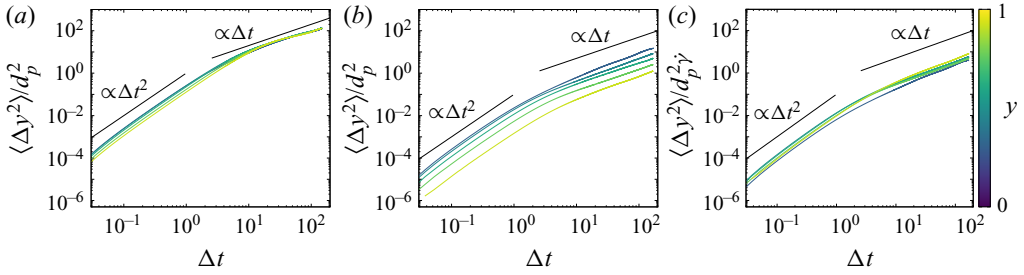


FIGURE 13. Particles’ mean squared displacement in the wall-normal direction (cf. (3.8)) normalized by the particle diameter squared $\langle \Delta y^2 \rangle / d_p^2$, for cases (a) W0P20 and (b,c) W25P20. In panel (c), the ordinate is also normalized by the mean shear rate of the streamwise fluid velocity $\dot{\gamma}$. The colours indicate different y locations of the reference particle at $\Delta t = 0$.

viscoelastic flow, $\langle \Delta y^2 \rangle$ is a stronger function of y during both the correlated and diffusive regimes. In the absence of the turbulence, it is expected that the particles’ dynamics is driven by shear-induced self-diffusion. We examine this hypothesis by normalizing $\langle \Delta y^2 \rangle$ with the mean shear rate of the streamwise fluid velocity, $\dot{\gamma}$, in figure 13(c). The better collapse of the curves corresponding to different y locations confirms that the shear-induced self-diffusion is a dominant mechanism for the dispersion of particles in the wall-normal direction.

In § 3.1, we have shown that the particles’ concentration increases away from the wall for $Wi \geq 5$ (cf. figure 4a). An explanation was sought by performing an additional simulation that probes the transient particles’ migration dynamics. The initial condition was a snapshot from the statistically stationary Newtonian particle-laden flow, where the particle concentration is almost flat in the majority of the channel. Viscoelasticity was then suddenly introduced, with $Wi = 25$. The particles migrated towards the channel centre over approximately 400 time units, and the migration velocity progressively weakened. The equilibrium concentration profile for case W25P20 was established beyond $t = 500$.

A particle in wall-bounded shear has an equilibrium position farther away from the wall when the carrier fluid is viscoelastic compared with Newtonian (e.g. Karnis & Mason (1966); Leshansky *et al.* (2007), and the Appendix). This lateral migration of isolated particles, or in the very dilute regime, is well documented and is due to an imbalance of elastic normal stresses (see D’Avino, Greco & Maffettone (2017), for a review). In the present concentrated suspension, interparticle collisions play an important role in shear-induced migration towards the channel centre. In order to elucidate the mechanism, the statistical measures introduced by Sundaram & Collins (1997) are tailored for our configuration. The propensity of particle interactions to affect a reference particle is determined by (i) the probability of the presence of a neighbouring particle and (ii) the intensity of their relative velocity. The first measure is quantified by the particle-pair distribution function, previously defined as q in (3.4). Here the quantity is redefined with a different normalization,

$$q'(r, \psi, \theta) = \langle dN(r, \psi, \theta) \rangle / (r^2 d\theta d\psi dr), \tag{3.9}$$

namely using the volume of the spherical bin, $r^2 d\theta d\psi dr$. Unlike the previous definition, $q'(r, \psi, \theta)$ is intentionally biased by the inhomogeneity of particles distribution in the wall-normal direction. As we will show shortly, this inhomogeneity plays an important role

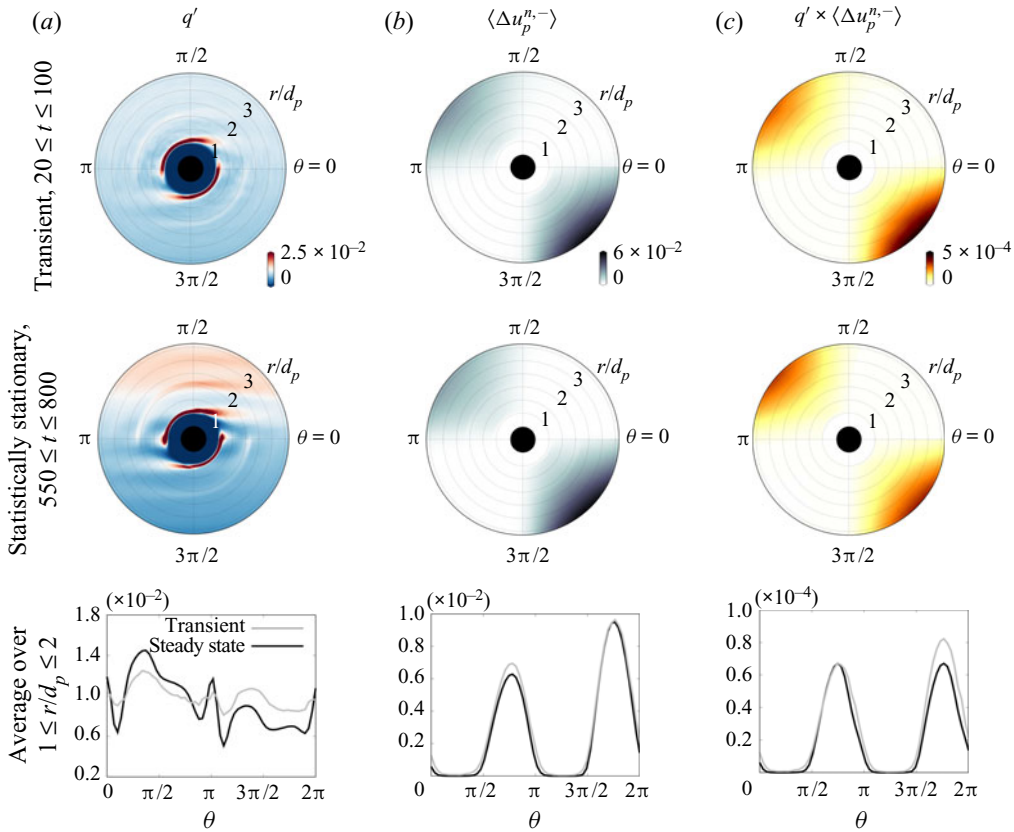


FIGURE 14. Measures of microstructure for case W25P20 and particles located at $0.6 \leq y \leq 0.8$, averaged during (top) transient and (middle) statistically stationary intervals. Lines compare the statistics averaged over $1 \leq r/d_p \leq 2$. (a) Particle-pair distribution function $q'(r, \psi, \theta)$ (3.9), (b) mean approaching velocity $\langle \Delta u_p^{n,-}(r, \psi, \theta) \rangle$ (3.10) and (c) intensity of particles collision measured by $q' \times \langle \Delta u_p^{n,-} \rangle$. All quantities are averaged over the polar angle range of $-\pi/8 < \psi - \pi/2 < \pi/8$.

in the migration dynamics. The second measure is expressed by the approaching velocity between the reference and a neighbouring particle m ,

$$\Delta u_p^{n,-}(r, \psi, \theta) = \frac{\sum_{m=1}^{N_p} \delta(r - |\mathbf{r}_m|) \delta(\psi - \psi_m) \delta(\theta - \theta_m) \Delta u_m^{n,-}}{dN(r, \psi, \theta)}, \tag{3.10}$$

$$\Delta u_m^{n,-} = \max \left\{ 0, -(\mathbf{u}_{p,m} - \mathbf{u}_{p,ref}) \cdot \frac{\mathbf{r}_m}{|\mathbf{r}_m|} \right\}. \tag{3.11}$$

On average, $\langle \Delta u_p^{n,-} \rangle(r, \psi, \theta)$ describes the spatial variations in the approaching velocity of neighbouring particles in the vicinity of the reference one. Finally, the product of q' and $\langle \Delta u_p^{n,-} \rangle$, referred to as the collision kernel when $r = d_p$ (Sundaram & Collins 1997), quantifies the intensity of collision events. Note that in addition to direct collisions, neighbouring particles also indirectly affect the motion of the reference one by

displacement of the interstitial fluid between them. Hence, the observable $q' \times \langle \Delta u_p^{n,-} \rangle$ will be examined even at $r > d_p$, with the knowledge that values at larger separation distances are less relevant to the dynamics of the reference particle.

These statistical measures are reported in [figure 14](#) for case W25P20. The figure compares the initial transient of the simulation and a statistically stationary interval. During the former, the profile of solid volume fraction is similar to its initial condition adopted from the Newtonian flow, i.e. it increases away from the wall at a relatively weak rate compared with its statistically stationary state. As a result, q' is slightly larger above the reference particle than below it during the transient, and this asymmetry becomes much more pronounced in the statistically stationary state ([figure 14a](#)). Due to the positive mean shear rate, neighbouring particles experience a finite approaching velocity only in regions Ω_2 and Ω_4 (cf. [figure 12a](#) for a definition). Also, the values of $\langle \Delta u_p^{n,-} \rangle$ are larger in Ω_4 due to the curvature of the mean streamwise velocity profile: the mean shear rate decreases away from the wall, giving rise to a stronger approaching velocity for neighbouring particles below the reference one ([figure 14b](#)). The combination of these two effects is shown in [figure 14\(c\)](#). While in the statistically stationary state $q' \times \langle \Delta u_p^{n,-} \rangle$ is symmetric about the origin, it is larger in Ω_4 during the initial transient. Hence, stronger collisions from below drive the reference particle towards the channel centre. In short, the curvature in mean streamwise velocity profile induces the migration of particles towards the channel centre, and this effect is eventually counterbalanced by the gradient of solid volume fraction in the wall-normal direction.

The results presented herein showed that, while both the presence of particles and viscoelasticity can suppress and even eradicate turbulence at moderate particle concentrations and high elasticity, drag can increase appreciably. Both the particle and polymer stresses become important in these conditions. The large contribution to the polymer stress takes place in the high-shear region of the flow, where the polymers undergo appreciable deformation in the vicinity of the particles, and decays in the channel centre. The particle contribution to the stress shifts away from the wall at higher Wi due to the change in the preferential migration of the particles.

4. Conclusion

Direct numerical simulations of particle-laden viscoelastic flow in a channel were performed at moderate particle concentration and a wide range of Weissenberg numbers, and the results were analysed in detail. The flow was resolved at the scale of particles with an immersed boundary method, and the viscoelastic effects were modelled by solving the evolution equations of the polymer conformation tensor for a FENE-P fluid. The particle-laden cases with a bulk solid volume fraction $\phi = 20\%$ were contrasted to their single-phase counterparts. Key features of the flow were also contrasted to data at dilute concentration ($\phi = 5\%$) from a previous study (Esteghamatian & Zaki 2019); differences are striking all the way from the global stress balance and down to the particle migration and microstructure.

In a regime where single-phase and dilute two-phase viscoelastic flows exhibit drag reduction with increasing elasticity, the concentrated suspension of particles leads to a non-monotonic change in drag. At low Weissenberg numbers, the turbulent shear stress is effectively reduced along with the total drag. Beyond $Wi = 5$, turbulence is nearly eradicated and the drag increases with increasing elasticity, due primarily to an increasing contribution from the polymer stress.

Consistent with the change in drag, the mean flow approaches the Poiseuille profile as the Weissenberg number approaches $Wi = 5$. Beyond that level, in the particle-laden flows, the mean flow flattens with further increase in elasticity. While this effect is reminiscent of the transition from laminar to elasto-inertial turbulence in single-phase viscoelastic flows (Choueiri, Lopez & Hof 2018), turbulence does not play a role here. The diagonal components of the Reynolds stresses, although highly suppressed, are still finite and are primarily driven by particle-induced perturbations which are insensitive to the level of elasticity. In addition, the shear component of Reynolds stresses is nearly eradicated, and quadrant analysis shows that each quadrant has nearly equal contribution to $u'_j v'_j$.

The influence of particles on the polymer stresses is examined by comparing the deformation and expansion of polymers in the single-phase and particle-laden conditions. Following Hameduddin & Zaki (2019), special care is exercised in characterizing the mean and deformations of the conformation tensor.

In the single-phase flow polymers are deformed in regions of the flow with high turbulence activity, while in the particle-laden case the strong polymer deformations and expansions are recorded in the vicinity of the particles' surfaces. By examining the particles microstructure, we showed that polymers are effectively perturbed in the straining regions near a reference particle, where the presence of neighbouring particles is less probable.

The dynamics of the particles was investigated by examining their diffusion and migration mechanism. Here too the findings are qualitatively different from the dilute case, where particles can promote the cycles of hibernating and active turbulence during which they synchronously migrate away from and towards the wall (Esteghamatian & Zaki 2019). In the present concentrated suspension and at the same level of elasticity, these cycles are entirely absent and the wall-normal particle mixing is markedly hindered due to the eradication of turbulence. A shear-induced self-diffusion is identified as the primary mechanism for mixing of particles in the viscoelastic conditions. In addition, transient migration towards the channel centre was observed exclusively in viscoelastic cases with $Wi \geq 5$ condition. Theoretical studies generally ascribe such migration trend to an imbalance in the particle-phase normal stresses (Morris 2009). We provided an explanation by comparing the microstructure and the collision statistics during the transient and statistically stationary stages of the simulations, starting from the Newtonian configuration and suddenly introducing viscoelasticity. The collision kernel shows that the curvature of the mean velocity profile leads to preferential migration towards the channel centre, which is counterbalanced by the gradient of solid volume fraction in the statistically stationary state.

Taken all together, at high elasticity and particle concentration, the migration pattern of the particles leads to clustering in the channel centre where the polymers in the interstitial space are inappreciably perturbed away from equilibrium. Yet, away from the channel centre, a significant increase in the polymer stresses is recorded near the particles' surfaces and becomes sufficiently large at high elasticity to ultimately cause an increase in the total drag – a reversal in the commonly anticipated effect of polymers.

Acknowledgements

This work was supported in part by the National Science Foundation (grant 1804004). Computational resources were provided by the Maryland Advanced Research Computing Center (MARCC).

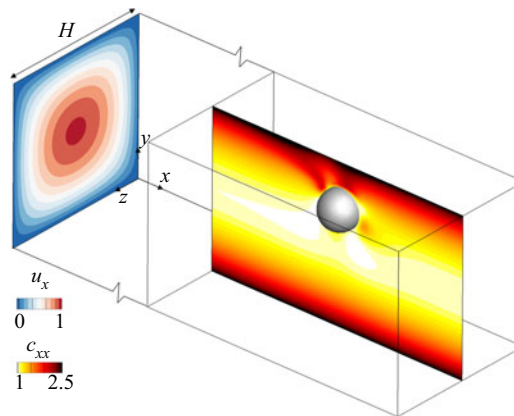


FIGURE 15. Configuration of validation test: lateral migration of a sphere in duct flow of Newtonian and Oldroyd-B fluids. No-slip boundary conditions $u_f = 0$ are imposed at $y = \{0, 1\}$ and $z = \{0, 1\}$, and periodicity is enforced in the x direction.

d_p/h	Re_c	β	Wi_c	y_{eq}/h	y_{eq}/h (Li <i>et al.</i> 2015)	Error %
0.25	18.9	1.0	0	0.773	0.776	0.39
			0.189	0.678	0.674	0.59
		0.1	0.567	0.5	0.5	0
			0.945	0.5	0.5	0

TABLE 2. Parameters of the simulations of isolated particle in duct flow and the final equilibrium positions.

Declaration of interests

The authors report no conflict of interest.

Appendix. Validation of the numerical algorithm

The particle-laden viscoelastic solver was extensively validated (see Esteghamatian & Zaki 2019). An additional validation case is presented here, where the lateral migration of a sphere in Newtonian and Oldroyd-B fluids is simulated and compared with data by Li, McKinley & Ardekani (2015). The computational domain is a duct geometry as illustrated in figure 15. The flow is periodic in x , and no-slip boundary conditions are imposed at $y = \{0, 1\}$ and $z = \{0, 1\}$. A neutrally buoyant sphere of diameter d_p is initially located at $(0 \times 0.75 \times 0.5)H$, where H is the height of the square channel. Computations were performed in a domain spanning over $16d_p$ and the particle blockage ratio is $d_p/H = 0.25$. The prescribed Reynolds number based on centre velocity is $Re_c \equiv U_c H/\nu = 18.9$, and the Weissenberg number and the viscosity ratio are $Wi_c = \lambda U_c/H$ and $\beta = 0.1$. The particles' equilibrium positions y_{eq} for three viscoelastic cases, $Wi_c = \{0.189, 0.567, 0.945\}$, are contrasted to the Newtonian condition in table 2. The results demonstrate the accuracy of our prediction of the particle migration and equilibrium condition.

REFERENCES

- AGARWAL, A., BRANDT, L. & ZAKI, T. A. 2014 Linear and nonlinear evolution of a localized disturbance in polymeric channel flow. *J. Fluid Mech.* **760**, 278–303.
- BECKER, L. E., MCKINLEY, G. H., RASMUSSEN, H. K. & HASSAGER, O. 1994 The unsteady motion of a sphere in a viscoelastic fluid. *J. Rheol.* **38** (2), 377–403.
- CHHABRA, R. P. 2006 *Bubbles, Drops, and Particles in non-Newtonian Fluids*. CRC.
- CHOUËIRI, G. H., LOPEZ, J. M. & HOF, B. 2018 Exceeding the asymptotic limit of polymer drag reduction. *Phys. Rev. Lett.* **120** (12), 124501.
- COSTA, P., PICANO, F., BRANDT, L. & BREUGEM, W. P. 2018 Effects of the finite particle size in turbulent wall-bounded flows of dense suspensions. *J. Fluid Mech.* **843**, 450–478.
- DAI, S. & TANNER, R. I. 2017 Elongational flows of some non-colloidal suspensions. *Rheol. Acta* **56** (1), 63–71.
- D’AVINO, G., GRECO, F. & MAFFETTONE, P. L. 2017 Particle migration due to viscoelasticity of the suspending liquid and its relevance in microfluidic devices. *Annu. Rev. Fluid Mech.* **49** (1), 341–360.
- D’AVINO, G. & MAFFETTONE, P. L. 2015 Particle dynamics in viscoelastic liquids. *J. Non-Newtonian Fluid Mech.* **215**, 80–104.
- DENN, M. M. & MORRIS, J. F. 2014 Rheology of non-Brownian suspensions. *Annu. Rev. Chem. Biomol. Engng* **5**, 203–228.
- DRAAD, A. A., KUIKEN, G. D. C. & NIEUWSTADT, F. T. M. 1998 Laminar–turbulent transition in pipe flow for Newtonian and non-Newtonian fluids. *J. Fluid Mech.* **377**, 267–312.
- DUBIEF, Y., TERRAPON, V. E., WHITE, C. M., SHAQFEH, E. S. G., MOIN, P. & LELE, S. K. 2005 New answers on the interaction between polymers and vortices in turbulent flows. *Flow Turbul. Combust.* **74** (4), 311–329.
- EINARSSON, J., YANG, M. & SHAQFEH, E. S. G. 2018 Einstein viscosity with fluid elasticity. *Phys. Rev. Fluids* **3** (1), 013301.
- ESTEGHAMATI, A. & ZAKI, T. A. 2019 Dilute suspension of neutrally buoyant particles in viscoelastic turbulent channel flow. *J. Fluid Mech.* **875**, 286–320.
- GLOWINSKI, R., PAN, T. W., HESLA, T. I., JOSEPH, D. D. & PÉRIAUX, J. 2001 A fictitious domain approach to the direct numerical simulation of incompressible viscous flow past moving rigid bodies: application to particulate flow. *J. Comput. Phys.* **169** (2), 363–426.
- GOYAL, N. & DERKSEN, J. J. 2012 Direct simulations of spherical particles sedimenting in viscoelastic fluids. *J. Non-Newtonian Fluid Mech.* **183–184**, 1–13.
- GROISMAN, A. & STEINBERG, V. 2000 Elastic turbulence in a polymer solution flow. *Nature* **405** (6782), 53–55.
- HAMEDUDDIN, I., GAYME, D. F. & ZAKI, T. A. 2019 Perturbative expansions of the conformation tensor in viscoelastic flows. *J. Fluid Mech.* **858**, 377–406.
- HAMEDUDDIN, I., MENEVEAU, C., ZAKI, T. A. & GAYME, D. F. 2018 Geometric decomposition of the conformation tensor in viscoelastic turbulence. *J. Fluid Mech.* **842**, 395–427.
- HAMEDUDDIN, I. & ZAKI, T. A. 2019 The mean conformation tensor in viscoelastic turbulence. *J. Fluid Mech.* **865**, 363–380.
- HAPPEL, J. & BRENNER, H. 2012 *Low Reynolds Number Hydrodynamics: with Special Applications to Particulate Media*, Vol. 1. Springer Science & Business Media.
- HWANG, W. R., HULSEN, M. A. & MEIJER, H. E. H. 2004 Direct simulations of particle suspensions in a viscoelastic fluid in sliding bi-periodic frames. *J. Non-Newtonian Fluid Mech.* **121** (1), 15–33.
- JEFFREY, D. J. & ACRIVOS, A. 1976 The rheological properties of suspensions of rigid particles. *AIChE J.* **22** (3), 417–432.
- KARNIS, A. & MASON, S. G. 1966 Particle motions in sheared suspensions. XIX. Viscoelastic media. *Trans. Soc. Rheol.* **10** (2), 571–592.
- KOCH, D. L. & SUBRAMANIAN, G. 2006 The stress in a dilute suspension of spheres suspended in a second-order fluid subject to a linear velocity field. *J. Non-Newtonian Fluid Mech.* **138** (2–3), 87–97.
- KULKARNI, P. M. & MORRIS, J. F. 2008 Suspension properties at finite Reynolds number from simulated shear flow. *Phys. Fluids* **20** (4), 040602.
- LEE, J., JUNG, S. Y., SUNG, H. J. & ZAKI, T. A. 2013 Effect of wall heating on turbulent boundary layers with temperature-dependent viscosity. *J. Fluid Mech.* **726**, 196–225.

- LEE, S. J. & ZAKI, T. A. 2017 Simulations of natural transition in viscoelastic channel flow. *J. Fluid Mech.* **820**, 232–262.
- LESHANSKY, A. M., BRANSKY, A., KORIN, N. & DINNAR, U. 2007 Tunable nonlinear viscoelastic “focusing” in a microfluidic device. *Phys. Rev. Lett.* **98** (23), 234501.
- LI, G., MCKINLEY, G. H. & ARDEKANI, A. M. 2015 Dynamics of particle migration in channel flow of viscoelastic fluids. *J. Fluid Mech.* **785**, 486–505.
- DE LILLO, F., BOFFETTA, G. & MUSACCHIO, S. 2012 Control of particle clustering in turbulence by polymer additives. *Phys. Rev. E* **85** (3), 1–6.
- LOISEL, V., ABBAS, M., MASBERNAT, O. & CLIMENT, E. 2013 The effect of neutrally buoyant finite-size particles on channel flows in the laminar-turbulent transition regime. *Phys. Fluids* **25** (12), 123304.
- MATAS, J.-P., MORRIS, J. F. & GUAZZELLI, E. 2003 Transition to turbulence in particulate pipe flow. *Phys. Rev. Lett.* **90** (1), 014501.
- MORRIS, J. F. 2009 A review of microstructure in concentrated suspensions and its implications for rheology and bulk flow. *Rheol. Acta* **48** (8), 909–923.
- NICOLAOU, L., JUNG, S. Y. & ZAKI, T. A. 2015 A robust direct-forcing immersed boundary method with enhanced stability for moving body problems in curvilinear coordinates. *Comput. Fluids* **119**, 101–114.
- NOWBAHAR, A., SARDINA, G., PICANO, F. & BRANDT, L. 2013 Turbophoresis attenuation in a turbulent channel flow with polymer additives. *J. Fluid Mech.* **732**, 706–719.
- PAGE, J. & ZAKI, T. A. 2014 Streak evolution in viscoelastic Couette flow. *J. Fluid Mech.* **742**, 520–521.
- PAGE, J. & ZAKI, T. A. 2015 The dynamics of spanwise vorticity perturbations in homogeneous viscoelastic shear flow. *J. Fluid Mech.* **777**, 327–363.
- PAGE, J. & ZAKI, T. A. 2016 Viscoelastic shear flow over a wavy surface. *J. Fluid Mech.* **801**, 392–429.
- PICANO, F., BREUGEM, W. P. & BRANDT, L. 2015 Turbulent channel flow of dense suspensions of neutrally buoyant spheres. *J. Fluid Mech.* **764**, 463–487.
- PICANO, F., BREUGEM, W.-P., MITRA, D. & BRANDT, L. 2013 Shear thickening in non-Brownian suspensions: an excluded volume effect. *Phys. Rev. Lett.* **111** (9), 098302.
- RAHMANI, M., HAMMOUTI, A. & WACHS, A. 2018 Momentum balance and stresses in a suspension of spherical particles in a plane Couette flow. *Phys. Fluids* **30** (4), 043301.
- ROSENFELD, M., KWAK, D. & VINOKUR, M. 1991 A fractional step solution method for the unsteady incompressible Navier–Stokes equations in generalized coordinate systems. *J. Comput. Phys.* **94** (1), 102–137.
- RUEDA, M. M., AUSCHER, M.-C., FULCHIRON, R., PERIE, T., MARTIN, G., SONNTAG, P. & CASSAGNAU, P. 2017 Rheology and applications of highly filled polymers: a review of current understanding. *Prog. Polym. Sci.* **66**, 22–53.
- SAMANTA, D., DUBIEF, Y., HOLZNER, M., SCHÄFER, C., MOROZOV, A. N., WAGNER, C. & HOF, B. 2013 Elasto-inertial turbulence. *Proc. Natl Acad. Sci. USA* **110** (26), 10557–10562.
- SCIROCCO, R., VERMANT, J. & MEWIS, J. 2005 Shear thickening in filled Boger fluids. *J. Rheol.* **49** (2), 551–567.
- SHAO, X., WU, T. & YU, Z. 2012 Fully resolved numerical simulation of particle-laden turbulent flow in a horizontal channel at a low Reynolds number. *J. Fluid Mech.* **693**, 319–344.
- STICKEL, J. J. & POWELL, R. L. 2005 Fluid mechanics and rheology of dense suspensions. *Annu. Rev. Fluid Mech.* **37**, 129–149.
- SUNDARAM, S. & COLLINS, L. R. 1997 Collision statistics in an isotropic particle-laden turbulent suspension. Part I. Direct numerical simulations. *J. Fluid Mech.* **335**, 75–109.
- TANNER, R. I. 2019 Rheology of noncolloidal suspensions with non-Newtonian matrices. *J. Rheol.* **63** (4), 705–717.
- TOMS, B. A. 1948 Some observations on the flow of linear polymer solutions through straight tubes at large Reynolds numbers. In *Proceedings of the 1st International Congress on Rheology*, pp. 135–141. North-Holland.
- WALLACE, J. M., ECKELMANN, H. & BRODKEY, R. S. 1972 The wall region in turbulent shear flow. *J. Fluid Mech.* **54** (1), 39–48.

- WHITE, C. M. & MUNGAL, M. G. 2008 Mechanics and prediction of turbulent drag reduction with polymer additives. *Annu. Rev. Fluid Mech.* **40** (1), 235–256.
- XI, L. & GRAHAM, M. D. 2010 Active and hibernating turbulence in minimal channel flow of Newtonian and polymeric fluids. *Phys. Rev. Lett.* **104**, 218–301.
- YANG, M. & SHAQFEH, E. S. G. 2018*a* Mechanism of shear thickening in suspensions of rigid spheres in Boger fluids. Part I: dilute suspensions. *J. Rheol.* **62** (6), 1363–1377.
- YANG, M. & SHAQFEH, E. S. G. 2018*b* Mechanism of shear thickening in suspensions of rigid spheres in Boger fluids. Part II: suspensions at finite concentration. *J. Rheol.* **62** (6), 1379–1396.
- ZADE, S., LUNDELL, F. & BRANDT, L. 2019 Turbulence modulation by finite-size spherical particles in Newtonian and viscoelastic fluids. *Intl J. Multiphase Flow* **112**, 116–129.
- ZARRAGA, I. E., HILL, D. A. & LEIGHTON, D. T. 2001 Normal stresses and free surface deformation in concentrated suspensions of noncolloidal spheres in a viscoelastic fluid. *J. Rheol.* **45** (5), 1065–1084.